

Calculation of intrinsic spin Hall conductivity by Wannier interpolation

Junfeng Qiao,^{1,2} Jiaqi Zhou,^{1,2} Zhe Yuan,³ and Weisheng Zhao^{1,2,*}

¹Fert Beijing Institute, BDBC, Beihang University, Beijing 100191, China

²School of Electronic and Information Engineering, Beihang University, Beijing 100191, China

³The Center for Advanced Quantum Studies and Department of Physics, Beijing Normal University, 100875 Beijing, China

(Dated: October 18, 2018)

Ab-initio calculation of intrinsic spin Hall conductivity (SHC) generally requires a strict convergence criterion and a dense k-point mesh to sample the Brillouin zone, making its convergence challenging and time-consuming. Here we present a scheme for efficiently and accurately calculating SHC based on maximally localized Wannier function (MLWF). The quantities needed by the Kubo formula of SHC are derived in the space of MLWF and it is shown that only the Hamiltonian, the overlap and the spin operator matrices are required from the initial *ab-initio* calculation. The computation of these matrices and the interpolation of Kubo formula on a dense k-point mesh can be easily achieved. We validate our results by prototypical calculations on fcc Pt and GaAs, which demonstrate that the Wannier interpolation approach is of high accuracy and efficiency. Calculations of α -Ta and β -Ta show that SHC of β -Ta is 2.7 times of α -Ta, while both have the opposite sign relative to fcc Pt and are an order of magnitude smaller than Pt. The calculated spin Hall angle of -0.156 , is quite consistent with previous experiment on β -Ta, further suggesting intrinsic contribution may dominate in β -Ta. Our approach could facilitate large-scale SHC calculations, and may benefit the discovery of materials with high intrinsic SHC.

I. INTRODUCTION

The spin Hall effect (SHE) is the phenomenon in which transverse pure spin current can be generated by applying an electric field [1]. In recent years, the utilization of SHE for the magnetization switching of magnetic tunnel junction has attracted lots of interest due to its potentially fast switching speed and low power consumption [2, 3]. SHE, together with other mechanisms like Rashba and Dresselhaus effects, give rise to the spin orbit torque (SOT) [4–6], which provides an alternative switching mechanism apart from spin transfer torque. The SHE can be separated into intrinsic SHE which is directly derived from relativistic band structure [7, 8], and extrinsic side-jump and skew-scattering SHE which are related to scattering [9]. The intrinsic SHE, significantly contributing to the total SHE in materials with strongly spin-orbit-coupled bands [1], can be calculated accurately based on *ab-initio* theories. According to the Kubo formula, the spin Hall conductivity (SHC) can be written as [10–12]

$$\sigma_{xy}^{\text{spin}z}(\omega) = \hbar \int_{\text{BZ}} \frac{d^3k}{(2\pi)^3} \sum_n f_{n\mathbf{k}} \times \sum_{m \neq n} \frac{2 \text{Im}[\langle n\mathbf{k} | \hat{j}_x^{\text{spin}z} | m\mathbf{k} \rangle \langle m\mathbf{k} | -e\hat{v}_y | n\mathbf{k} \rangle]}{(\epsilon_{n\mathbf{k}} - \epsilon_{m\mathbf{k}})^2 - (\hbar\omega + i\eta)^2}, \quad (1)$$

where n, m are band indexes, ϵ_n, ϵ_m are the eigenvalues, $f_{n\mathbf{k}}$ is the Fermi distribution function, BZ is the first Brillouin zone, $\hat{j}_x^{\text{spin}z} = \frac{1}{2}\{\hat{s}_z, \hat{v}_x\}$ is the spin current operator

and $\hat{s}_z = \frac{\hbar}{2}\hat{\sigma}_z$ is the spin operator, $\hat{v}_y = \frac{1}{\hbar} \frac{\partial H(\mathbf{k})}{\partial k_y}$ is the velocity operator and the frequency ω and η are set to zero in the direct current (dc) clean limit.

The calculation of SHC can be performed by direct evaluation of Equ. (1) or its equivalent form on the *ab-initio* wave function, which could be acquired by plane wave (PW) or all-electron linear muffin-tin orbital method (LMTO) [13–15]. However, these kinds of direct evaluations are very time-demanding, usually an extremely dense k-point mesh (k-mesh) on the order of one million is needed [15]. Another available approach is evaluating Equ.(1) on a set of tight-binding parameters [16]. Efficient as well as fully *ab-initio* evaluation of Equ.(1) is in urgent need.

To mitigate this problem, the direct evaluation of Kubo formula should be avoided. Anomalous Hall effect (AHE) is a phenomenon closely related to SHE, and a very successful scheme for the evaluation of anomalous Hall conductivity (AHC) has been developed [17] based on maximally localized Wannier function (MLWF), which utilizes the remaining gauge freedom of the Bloch function [18, 19]. With an unitary gauge transformation, the discontinuous Bloch gauge is transformed into a smooth Wannier gauge. Followed by a Fourier transformation, the real space Hamiltonian and other quantities can be constructed, which are localized in real space because of the smoothness of Wannier gauge. The maximally localized real space quantities thus enable the interpolation on arbitrary dense k-mesh. The Wannier approach is both efficient and accurate, since in essence MLWF can be viewed as a tight-binding basis while at the same time preserves the accuracy of *ab-initio* calculation in the energy window of interest, due to its real space maximally localization. Inspired by the method for AHC, we derived the formulas for the evaluation of SHC based on

* weisheng.zhao@buaa.edu.cn

Wannier interpolation.

The Wannier interpolation approach for calculating SHC is composed of two parts: the construction of MLWF from *ab-initio* wave function and the calculation of SHC based on MLWF. Generally, only a relatively coarse k-mesh *ab-initio* calculation is enough for the construction of MLWF. Afterwards, the interpolation of needed quantities on a dense k-mesh can be easily achieved with moderate computational burden.

The paper is organized as follows. In Sec.II we describe the basic theories and introduce the essential quantities we need to evaluate in our Wannier-based approach. In Sec.III we provide the detailed derivations on the MLWF basis. To validate our approach, exemplary calculations of Pt and GaAs are shown in Sec.IV A and IV B. Sec.IV C describes SHC calculations of α -Ta and β -Ta. Finally, Sec.V contains a brief summary.

II. DEFINITIONS AND BACKGROUND

First we give a basic description of Kubo formula for SHC. Since the Wannier interpolation approach for AHC has been well established, a comparison of SHC and AHC is beneficial. Then we provide a brief and self-contained introduction to the MLWF. More details on MLWF can be found in Ref. [18–20].

A. Kubo formula

The general form of Kubo formula for AHC and SHC is given by [12–14]

$$\sigma_{xy}(\omega) = \frac{\hbar}{VN_k^3} \sum_{\mathbf{k}} \sum_n f_{n\mathbf{k}} \times \sum_{m \neq n} \frac{2 \text{Im}[\langle n\mathbf{k} | \hat{j}_x | m\mathbf{k} \rangle \langle m\mathbf{k} | -e\hat{v}_y | n\mathbf{k} \rangle]}{(\epsilon_{n\mathbf{k}} - \epsilon_{m\mathbf{k}})^2 - (\hbar\omega + i\eta)^2}, \quad (2)$$

where $\hat{j}_x = -e\hat{v}_x, \frac{1}{2}\{\hat{s}_z, \hat{v}_x\}$ for AHC and SHC, respectively. Here the integral in Equ.(1) is replaced by numerical sum, and V is the primitive cell volume, N_k^3 is the number of k-points in the BZ. The SHC is multiplied by $\frac{-2e}{\hbar}$ to convert it into the unit of S/length, the same as that of AHC. Comparing the Kubo formulas for AHC and SHC, the only difference is the spin current operator matrix elements $\langle n\mathbf{k} | \hat{j}_x^{\text{spin}} | m\mathbf{k} \rangle$, which is the key quantity we need to evaluate.

To facilitate further analysis, we separate the Equ.(2) into the band-projected Berry curvature-like term

$$\Omega_{n,xy}^{\text{spin}}(\mathbf{k}) = \hbar^2 \sum_{m \neq n} \frac{-2 \text{Im}[\langle n\mathbf{k} | \frac{1}{2}\{\hat{\sigma}_z, \hat{v}_x\} | m\mathbf{k} \rangle \langle m\mathbf{k} | \hat{v}_y | n\mathbf{k} \rangle]}{(\epsilon_{n\mathbf{k}} - \epsilon_{m\mathbf{k}})^2 - (\hbar\omega + i\eta)^2} \quad (3)$$

and the SHC is the sum over occupied bands

$$\sigma_{xy}^{\text{spin}}(\omega) = -\frac{e^2}{\hbar} \frac{1}{VN_k^3} \sum_{\mathbf{k}} \sum_n f_{n\mathbf{k}} \Omega_{n,xy}^{\text{spin}}(\mathbf{k}). \quad (4)$$

The unit of the $\Omega_{n,xy}^{\text{spin}}(\mathbf{k})$ is length², and the unit of $\sigma_{xy}^{\text{spin}}$ is $\frac{e^2}{\hbar} \frac{1}{\text{length}}$ [note $\frac{e^2}{\hbar} \simeq 2.434 \times 10^{-4}$ S]. To convert into the unit $\frac{\hbar}{e}$ S/length, the $\sigma_{xy}^{\text{spin}}$ should be multiplied by $\frac{\hbar}{-2e}$. The case of $\omega = 0$ corresponds to dc SHC while that of $\omega \neq 0$ corresponds to alternating current (ac) SHC.

B. Wannier interpolation

1. Construction of MLWF

The Kohn-Sham equation for the periodic part of the Bloch function is written as

$$\hat{H}_{\mathbf{k}} u_{n\mathbf{k}} = \epsilon_{n\mathbf{k}} u_{n\mathbf{k}}, \quad (5)$$

where \mathbf{k} is the k-point vector, n is the band index, $u_{n\mathbf{k}}(\mathbf{r}) = e^{-i\mathbf{k}\mathbf{r}} \psi_{n\mathbf{k}}(\mathbf{r})$ is the periodic part of the Bloch function $\psi_{n\mathbf{k}}(\mathbf{r})$. $\hat{H}_{\mathbf{k}}$ is the transformed Hamiltonian $\hat{H}_{\mathbf{k}} = e^{-i\mathbf{k}\mathbf{r}} \hat{H} e^{i\mathbf{k}\mathbf{r}}$ and $\epsilon_{n\mathbf{k}}$ is the eigenvalue.

Usually one needs a lot of plane waves to expand the $u_{n\mathbf{k}}$ in PW method and the diagonalization of the Hamiltonian matrix is performed on each k-point. An alternative representation is the real space Wannier function $|\mathbf{R}n\rangle$, which can be viewed as the Fourier transform of the Bloch wave function

$$|\mathbf{R}n\rangle = \frac{V}{(2\pi)^3} \int_{\text{BZ}} d\mathbf{k} e^{-i\mathbf{k}\cdot\mathbf{R}} |\psi_{n\mathbf{k}}\rangle, \quad (6)$$

where V is the volume of the real-space primitive cell and BZ is the Brillouin zone.

In principle, a smooth function in real space results in a localized function in its reciprocal space, and vice versa. However, it is not naturally guaranteed that the simply summed Bloch function of Equ. (6) results in a smooth function $|\mathbf{R}n\rangle$ in real space. Fortunately, there is a gauge freedom left in the definition of Bloch function, we can replace $|\psi_{n\mathbf{k}}\rangle$ by

$$|\tilde{\psi}_{n\mathbf{k}}\rangle = e^{i\varphi_n(\mathbf{k})} |\psi_{n\mathbf{k}}\rangle, \quad (7)$$

or equivalently,

$$|\tilde{u}_{n\mathbf{k}}\rangle = e^{i\varphi_n(\mathbf{k})} |u_{n\mathbf{k}}\rangle \quad (8)$$

without changing the physical description of the system. The $\varphi_n(\mathbf{k})$ can be any real function that is periodic in reciprocal space [20]. We can utilize this freedom to construct localized WFs in real space, the so-called maximally localized Wannier function.

We define the J dimensional unitary transformation $\mathcal{U}(\mathbf{k})$ which takes the original Bloch function $|u_{n\mathbf{k}}^{(0)}\rangle$ to

the smoothed function $|\tilde{u}_{n\mathbf{k}}\rangle$ as

$$|\tilde{u}_{n\mathbf{k}}\rangle = \sum_{m=1}^J |u_{m\mathbf{k}}^{(0)}\rangle \mathcal{U}_{mn}(\mathbf{k}), \quad (9)$$

where J is the number of states need to be considered for our targeted physical properties. We call this unitary transformation as the transformation from Bloch gauge to Wannier gauge. Thus, the Fourier transformation pair between the smoothed Bloch functions and the MLWFs are

$$\begin{aligned} |\mathbf{R}n\rangle &= \frac{1}{N_k^3} \sum_{\mathbf{k}} e^{-i\mathbf{k}\cdot\mathbf{R}} |\tilde{u}_{n\mathbf{k}}\rangle, \\ \Updownarrow \\ |\tilde{u}_{n\mathbf{k}}\rangle &= \sum_{\mathbf{R}} e^{i\mathbf{k}\cdot\mathbf{R}} |\mathbf{R}n\rangle, \end{aligned} \quad (10)$$

where N_k^3 is the number of points in BZ.

The above mentioned procedure is suitable for a group of isolated bands [18], e.g. the occupied valence bands of an insulator. However, for entangled bands, a process called disentanglement should be adopted [19], in which J smoothly varying $|\tilde{u}_{n\mathbf{k}}\rangle$ are extracted from $\mathcal{J}_{\mathbf{k}} > J$ original Bloch bands, where $\mathcal{J}_{\mathbf{k}}$ can be varied throughout the BZ. Using a set of J localized trial orbitals $g_n(r)$ and projecting them onto the original Bloch states

$$|\phi_{n\mathbf{k}}\rangle = \sum_{m=1}^{\mathcal{J}_{\mathbf{k}}} |\psi_{m\mathbf{k}}^{(0)}\rangle \langle \psi_{m\mathbf{k}}^{(0)} | g_n \rangle, \quad (11)$$

after normalization

$$|\psi_{m\mathbf{k}}\rangle = \sum_{m=1}^J |\phi_{m\mathbf{k}}\rangle (S_{\mathbf{k}}^{-1/2})_{mn} \quad (12)$$

we acquire a set of J smooth Bloch-like states. The overlap matrix $(A_{\mathbf{k}})_{mn} = \langle \psi_{m\mathbf{k}} | g_n \rangle$ is of dimension $\mathcal{J}_{\mathbf{k}} \times J$ and $(S_{\mathbf{k}})_{mn} = \langle \phi_{m\mathbf{k}} | \phi_{n\mathbf{k}} \rangle_V = (A_{\mathbf{k}}^\dagger A_{\mathbf{k}})_{mn}$ where $A_{\mathbf{k}}^\dagger$ is the conjugate transpose of $A_{\mathbf{k}}$. Other than projecting onto the trial orbitals $g_n(r)$, we can adopt an iterative method to obtain an optimally smooth space of J Bloch-like states at each \mathbf{k} which are the linear combinations of the original $\mathcal{J}_{\mathbf{k}}$ states.

In summary, by disentanglement we construct an optimally smooth space of J Bloch-like states from initial $\mathcal{J}_{\mathbf{k}}$ Bloch states. Then by a gauge-selection step we obtain J individually smooth Wannier gauge states. From now on we write the smooth varying $|\tilde{u}_{n\mathbf{q}}\rangle$ as $|u_{n\mathbf{q}}^{(W)}\rangle$ to be consistent with latter derivations, and we use \mathbf{q} rather than \mathbf{k} to represent the k-point of the initial *ab-initio* k-mesh, while the \mathbf{k} symbol is reserved for the Wannier interpolation k-mesh used in the following steps. The combined result is

$$|\psi_{n\mathbf{q}}^{(W)}\rangle = \sum_{m=1}^{\mathcal{J}_{\mathbf{q}}} |\psi_{m\mathbf{q}}^{(0)}\rangle V_{\mathbf{q},mn}. \quad (13)$$

Here, $V_{\mathbf{q},mn}$ is a $\mathcal{J}_{\mathbf{k}} \times J$ dimensional matrix.

2. Wannier interpolation of Hamiltonian matrix

After MLWF has been constructed, we interpolate operators on a dense k-mesh to get a converged result. In this section we use the interpolation of the Hamiltonian matrix $H_{nm}(\mathbf{k}) = \langle \psi_{n\mathbf{k}} | \hat{H} | \psi_{m\mathbf{k}} \rangle$ as an example to illustrate the key ideas behind Wannier interpolation.

For the reciprocal space Hamiltonian operator $\hat{H}(\mathbf{q})$, we define the $J \times J$ Hamiltonian matrix in the Wannier gauge as

$$H_{nm}^{(W)}(\mathbf{q}) = \langle u_{n\mathbf{q}}^{(W)} | \hat{H}(\mathbf{q}) | u_{m\mathbf{q}}^{(W)} \rangle = [V^\dagger(\mathbf{q}) H^{(0)}(\mathbf{q}) V(\mathbf{q})]_{nm}, \quad (14)$$

where $H_{nm}^{(0)}(\mathbf{q}) = \mathcal{E}_{n\mathbf{q}}^{(0)} \delta_{nm}$ is the diagonal Hamiltonian matrix of the original Bloch states, δ_{nm} is the Kronecker delta function. If diagonalizing $H_{nm}^{(W)}(\mathbf{q})$ by

$$U^\dagger(\mathbf{q}) H^{(W)}(\mathbf{q}) U(\mathbf{q}) = H^{(H)}(\mathbf{q}), \quad (15)$$

where $H_{nm}^{(H)}(\mathbf{q}) = \mathcal{E}_{n\mathbf{q}}^{(H)} \delta_{nm}$, then $\mathcal{E}_{n\mathbf{q}}^{(H)}$ will be identical to the original *ab-initio* $\mathcal{E}_{n\mathbf{q}}^{(0)}$ in the range of $n = 1, 2, \dots, J$. Transforming the Hamiltonian operator from reciprocal space to real space,

$$H_{nm}^{(W)}(\mathbf{R}) = \frac{1}{N_q^3} \sum_{\mathbf{q}} e^{-i\mathbf{q}\cdot\mathbf{R}} H_{nm}^{(W)}(\mathbf{q}), \quad (16)$$

and then performing inverse Fourier transform

$$H_{nm}^{(W)}(\mathbf{k}) = \sum_{\mathbf{R}} e^{i\mathbf{k}\cdot\mathbf{R}} H_{nm}^{(W)}(\mathbf{R}), \quad (17)$$

we succeed in interpolating the Hamiltonian operator on arbitrary k-point \mathbf{k} .

Since the Wannier functions (WF) we chose are maximally localized, the $H_{nm}^{(W)}(\mathbf{R})$ is expected to be well localized in real space, a few \mathbf{R} are sufficient in the sum of Equ. (17).

The final step is to diagonalize $H_{nm}^{(W)}(\mathbf{k})$,

$$U^\dagger(\mathbf{k}) H^{(W)}(\mathbf{k}) U(\mathbf{k}) = H^{(H)}(\mathbf{k}), \quad (18)$$

then the acquired eigenvalues and gauge transformation matrix $U(\mathbf{k})$ on arbitrary k-point \mathbf{k} can be used for latter extractions of the targeted physical properties. We comment here that since $H^{(W)}(\mathbf{k})$ are of dimensions $J \times J$, their diagonalizations are very ‘‘cheap’’, compared with the diagonalizations of the Hamiltonian matrices in PW method.

Apart from the Hamiltonian matrix $\langle \psi_{m\mathbf{k}} | \hat{H} | \psi_{n\mathbf{k}} \rangle$, another useful quantity for the calculation of SHC is the velocity operator matrix $\langle \psi_{m\mathbf{k}} | \hat{v}_y | \psi_{n\mathbf{k}} \rangle$. By using integration by parts, we arrive at

$$\begin{aligned} \langle \psi_{m\mathbf{k}} | \hat{v}_y | \psi_{n\mathbf{k}} \rangle &= \frac{1}{\hbar} \langle \psi_{m\mathbf{k}} | \frac{\partial \hat{H}_{\mathbf{k}}}{\partial \mathbf{k}_y} | \psi_{n\mathbf{k}} \rangle \\ &= \frac{1}{\hbar} \frac{\partial \mathcal{E}_{n\mathbf{k}}}{\partial \mathbf{k}_y} \delta_{mn} + \frac{i}{\hbar} (\mathcal{E}_{m\mathbf{k}} - \mathcal{E}_{n\mathbf{k}}) A_{mn,y}(\mathbf{k}), \end{aligned} \quad (19)$$

$$A_{mn,y}(\mathbf{k}) = i\langle u_{m\mathbf{k}} | \partial_y u_{n\mathbf{k}} \rangle, \quad (20)$$

where $\partial_y = \frac{\partial}{\partial k_y}$. The Wannier interpolation of the matrix $A_{mn,y}$ has been developed in the calculation of AHC, detailed derivations can be found in Ref. [17]

III. DERIVATION OF SHC FOR WANNIER INTERPOLATION

Expanding the spin current operator as $\hat{j}_x^{\text{spin}z} = \frac{1}{2}(\hat{s}_z \hat{v}_x + \hat{v}_x \hat{s}_z)$, since $\langle \psi_{n\mathbf{k}} | \hat{s}_z \hat{v}_x | \psi_{m\mathbf{k}} \rangle^* = \langle \psi_{m\mathbf{k}} | (\hat{s}_z \hat{v}_x)^\dagger | \psi_{n\mathbf{k}} \rangle = \langle \psi_{m\mathbf{k}} | \hat{v}_x \hat{s}_z | \psi_{n\mathbf{k}} \rangle$, we define

$$B_{nm}(\mathbf{k}) = \langle \psi_{n\mathbf{k}} | \hat{s}_z \hat{v}_x | \psi_{m\mathbf{k}} \rangle, \quad (21)$$

thus

$$\langle \psi_{n\mathbf{k}} | \hat{j}_x^{\text{spin}z} | \psi_{m\mathbf{k}} \rangle = \frac{1}{2} [B(\mathbf{k}) + B^+(\mathbf{k})]_{nm}. \quad (22)$$

Considering the velocity operator $\hat{v}_x = \frac{1}{\hbar} \frac{\partial H(\mathbf{k})}{\partial k_x}$ and using integration by parts, we arrive at

$$\begin{aligned} B_{nm}(\mathbf{k}) &= \frac{1}{\hbar} \frac{\partial \mathcal{E}_{m\mathbf{k}}}{\partial k_x} \langle u_{n\mathbf{k}} | \hat{s}_z | u_{m\mathbf{k}} \rangle \\ &\quad + \frac{\mathcal{E}_{m\mathbf{k}}}{\hbar} \langle u_{n\mathbf{k}} | \hat{s}_z | \partial_x u_{m\mathbf{k}} \rangle \\ &\quad - \frac{1}{\hbar} \langle u_{n\mathbf{k}} | \hat{s}_z \hat{H}_{\mathbf{k}} | \partial_x u_{m\mathbf{k}} \rangle. \end{aligned} \quad (23)$$

For the simplicity of latter derivations, we define

$$S_{nm}^{(H)}(\mathbf{k}) = \langle u_{n\mathbf{k}}^{(H)} | \hat{s}_z | u_{m\mathbf{k}}^{(H)} \rangle, \quad (24)$$

$$K_{nm}^{(H)}(\mathbf{k}) = \langle u_{n\mathbf{k}}^{(H)} | \hat{s}_z | \partial_x u_{m\mathbf{k}}^{(H)} \rangle, \quad (25)$$

$$L_{nm}^{(H)}(\mathbf{k}) = \langle u_{n\mathbf{k}}^{(H)} | \hat{s}_z \hat{H}_{\mathbf{k}} | \partial_x u_{m\mathbf{k}}^{(H)} \rangle, \quad (26)$$

where the superscript (H) serves as a reminder that these $|u_{n\mathbf{k}}^{(H)}\rangle$ lie in the Bloch gauge. In short,

$$B_{nm}^{(H)}(\mathbf{k}) = \frac{1}{\hbar} \frac{\partial \mathcal{E}_{m\mathbf{k}}}{\partial k_x} S_{nm}^{(H)}(\mathbf{k}) + \frac{\mathcal{E}_{m\mathbf{k}}}{\hbar} K_{nm}^{(H)}(\mathbf{k}) - \frac{1}{\hbar} L_{nm}^{(H)}(\mathbf{k}). \quad (27)$$

Then we need to transform to Wannier gauge by using

$$|u_{n\mathbf{k}}^{(H)}\rangle = \sum_m |u_{m\mathbf{k}}^{(W)}\rangle U_{mn}. \quad (28)$$

Substituting Equ.(28) into Equ.(24) (25) (26), we arrive at

$$S^{(H)} = U^+ \langle u^{(W)} | \hat{s}_z | u^{(W)} \rangle U, \quad (29)$$

$$\begin{aligned} K^{(H)} &= U^+ \langle u^{(W)} | \hat{s}_z | \partial_x u^{(W)} \rangle U \\ &\quad + U^+ \langle u^{(W)} | \hat{s}_z | u^{(W)} \rangle U D_x^{(H)}, \end{aligned} \quad (30)$$

$$\begin{aligned} L^{(H)} &= U^+ \langle u^{(W)} | \hat{s}_z \hat{H} | \partial_x u^{(W)} \rangle U \\ &\quad + U^+ \langle u^{(W)} | \hat{s}_z \hat{H} | u^{(W)} \rangle U D_x^{(H)}, \end{aligned} \quad (31)$$

where

$$D_x^{(H)} = U^+ \partial_x U, \quad (32)$$

and the $D_x^{(H)}$ has been computed in the calculation of velocity operator. From now on the subscript nm and the k-point \mathbf{k} are omitted for conciseness and matrix multiplication are implied.

To evaluate the Wannier gauge matrices like $\langle u^{(W)} | \hat{s}_z | u^{(W)} \rangle$, we need to transform $|u_{n\mathbf{k}}^{(W)}\rangle$ into its real space representation $|\mathbf{R}n\rangle$

$$|\mathbf{R}n\rangle = \frac{1}{N_k^3} \sum_{\mathbf{k}} e^{i\mathbf{k}(\mathbf{r}-\mathbf{R})} |u_{n\mathbf{k}}^{(W)}\rangle \quad (33)$$

by its inverse Fourier transform

$$|u_{n\mathbf{k}}^{(W)}\rangle = \sum_{\mathbf{R}} e^{-i\mathbf{k}(\mathbf{r}-\mathbf{R})} |\mathbf{R}n\rangle. \quad (34)$$

The maximal localization ensures that a minimum set of nearest neighbor \mathbf{R} -points is sufficient for the inverse Fourier transform Equ.(34), which enables the accurate interpolation of wave function on arbitrary k-point. This is the core function of MLWF and accounts for its successful evaluation of many physical quantities such as AHC [17], orbital magnetization [21], and etc. [22]

Substituting Equ.(34) to the Wannier gauge matrices, we arrive at

$$\langle u_{\mathbf{k}}^{(W)} | \hat{s}_z | u_{\mathbf{k}}^{(W)} \rangle = \sum_{\mathbf{R}} e^{i\mathbf{k}\mathbf{R}} \langle \mathbf{0} | \hat{s}_z | \mathbf{R} \rangle, \quad (35)$$

$$\langle u_{\mathbf{k}}^{(W)} | \hat{s}_z | \partial_x u_{\mathbf{k}}^{(W)} \rangle = -i \sum_{\mathbf{R}} e^{i\mathbf{k}\mathbf{R}} \langle \mathbf{0} | \hat{s}_z (\mathbf{r} - \mathbf{R})_x | \mathbf{R} \rangle, \quad (36)$$

$$\langle u_{\mathbf{k}}^{(W)} | \hat{s}_z \hat{H} | \partial_x u_{\mathbf{k}}^{(W)} \rangle = -i \sum_{\mathbf{R}} e^{i\mathbf{k}\mathbf{R}} \langle \mathbf{0} | \hat{s}_z \hat{H} (\mathbf{r} - \mathbf{R})_x | \mathbf{R} \rangle, \quad (37)$$

$$\langle u_{\mathbf{k}}^{(W)} | \hat{s}_z \hat{H} | u_{\mathbf{k}}^{(W)} \rangle = \sum_{\mathbf{R}} e^{i\mathbf{k}\mathbf{R}} \langle \mathbf{0} | \hat{s}_z \hat{H} | \mathbf{R} \rangle. \quad (38)$$

The quantities need to be evaluated are the four real space matrices $\langle \mathbf{0} | \hat{s}_z | \mathbf{R} \rangle$, $\langle \mathbf{0} | \hat{s}_z (\mathbf{r} - \mathbf{R})_x | \mathbf{R} \rangle$, $\langle \mathbf{0} | \hat{s}_z \hat{H} (\mathbf{r} - \mathbf{R})_x | \mathbf{R} \rangle$ and $\langle \mathbf{0} | \hat{s}_z \hat{H} | \mathbf{R} \rangle$.

These real space matrices can be evaluated on the original coarse *ab-initio* k-mesh, and we use the notation $|u_{n\mathbf{q}}^{(0)}\rangle$, $|u_{n\mathbf{k}}^{(H)}\rangle$, $|u_{n\mathbf{k}}^{(W)}\rangle$ and $|\mathbf{R}n\rangle$ to represent the original *ab-initio* Bloch wave function, the Hamiltonian gauge

wave function, the Wannier gauge wave function and the smooth real space Wannier wave function, respectively. The notation \mathbf{q} and \mathbf{k} are used to differentiate the coarse *ab-initio* \mathbf{q} mesh with the dense Wannier interpolation \mathbf{k} mesh.

The four real space matrices are evaluated in the original *ab-initio* space. The transformation from coarse *ab-initio* \mathbf{q} -mesh to real space mesh are summarized as follows,

$$|u_{n\mathbf{q}}^{(W)}\rangle = \sum_m |u_{m\mathbf{q}}^{(0)}\rangle V_{\mathbf{q},mn}, \quad (39)$$

$$|u_{n\mathbf{q}}^{(H)}\rangle = \sum_m |u_{m\mathbf{q}}^{(W)}\rangle U_{mn}, \quad (40)$$

$$|\mathbf{R}n\rangle = \frac{1}{N_q^3} \sum_{\mathbf{q}} e^{i\mathbf{q}(\mathbf{r}-\mathbf{R})} |u_{n\mathbf{q}}^{(W)}\rangle, \quad (41)$$

where N_q^3 is the total number of \mathbf{q} -points on the coarse \mathbf{q} -mesh. The density of \mathbf{q} -mesh should be sufficient that high quality $|\mathbf{R}n\rangle$ can be constructed.

From the real space Wannier function $|\mathbf{R}n\rangle$, the real space matrices can be readily evaluated,

$$\langle \mathbf{0} | \hat{s}_z | \mathbf{R} \rangle = \frac{1}{N_q^3} \sum_{\mathbf{q}} e^{-i\mathbf{q}\mathbf{R}} \langle u_{\mathbf{q}}^{(W)} | \hat{s}_z | u_{\mathbf{q}}^{(W)} \rangle, \quad (42)$$

$$\langle \mathbf{0} | \hat{s}_z (\mathbf{r} - \mathbf{R})_x | \mathbf{R} \rangle = i \frac{1}{N_q^3} \sum_{\mathbf{q}} e^{-i\mathbf{q}\mathbf{R}} \langle u_{\mathbf{q}}^{(W)} | \hat{s}_z | \partial_x u_{\mathbf{q}}^{(W)} \rangle, \quad (43)$$

$$\langle \mathbf{0} | \hat{s}_z \hat{H} (\mathbf{r} - \mathbf{R})_x | \mathbf{R} \rangle = i \frac{1}{N_q^3} \sum_{\mathbf{q}} e^{-i\mathbf{q}\mathbf{R}} \langle u_{\mathbf{q}}^{(W)} | \hat{s}_z \hat{H} | \partial_x u_{\mathbf{q}}^{(W)} \rangle, \quad (44)$$

$$\langle \mathbf{0} | \hat{s}_z \hat{H} | \mathbf{R} \rangle = \frac{1}{N_q^3} \sum_{\mathbf{q}} e^{-i\mathbf{q}\mathbf{R}} \langle u_{\mathbf{q}}^{(W)} | \hat{s}_z \hat{H} | u_{\mathbf{q}}^{(W)} \rangle. \quad (45)$$

The evaluation of the needed matrices in Equ.(42) and (45) is fairly simple by using Equ.(39),

$$\langle u_{\mathbf{q}}^{(W)} | \hat{s}_z | u_{\mathbf{q}}^{(W)} \rangle = V_{\mathbf{q}}^+ S_{\mathbf{q}}^{(0)} V_{\mathbf{q}}, \quad (46)$$

and

$$\langle u_{\mathbf{q}}^{(W)} | \hat{s}_z \hat{H} | u_{\mathbf{q}}^{(W)} \rangle = V_{\mathbf{q}}^+ S_{\mathbf{q}}^{(0)} H_{\mathbf{q}}^{(0)} V_{\mathbf{q}}. \quad (47)$$

The evaluation of the needed matrices in Equ.(43) and (44) utilize the smoothness of $|u_{\mathbf{q}}^{(W)}\rangle$. We expand the $|\partial_x u_{\mathbf{q}}^{(W)}\rangle$ as [18]

$$|\partial_x u_{\mathbf{q}}^{(W)}\rangle = \sum_{\mathbf{b}_x} w_{\mathbf{b}_x} \mathbf{b}_x [u_{\mathbf{q}+\mathbf{b}_x}^{(W)} - u_{\mathbf{q}}^{(W)}], \quad (48)$$

where \mathbf{b} is a vector connecting a \mathbf{q} point to its near neighbors and together with its weight $w_{\mathbf{b}}$ satisfy the completeness relation Ref. [18] Equ.(B1). Thus,

$$\begin{aligned} & \langle u_{\mathbf{q}}^{(W)} | \hat{s}_z | \partial_x u_{\mathbf{q}}^{(W)} \rangle \\ &= \sum_{\mathbf{b}_x} w_{\mathbf{b}_x} \mathbf{b}_x [V_{\mathbf{q}}^+ \langle u_{\mathbf{q}}^{(0)} | \hat{s}_z | u_{\mathbf{q}+\mathbf{b}_x}^{(0)} \rangle V_{\mathbf{q}+\mathbf{b}_x} \\ & \quad - V_{\mathbf{q}}^+ \langle u_{\mathbf{q}}^{(0)} | \hat{s}_z | u_{\mathbf{q}}^{(0)} \rangle V_{\mathbf{q}}] \\ &= \sum_{\mathbf{b}_x} w_{\mathbf{b}_x} \mathbf{b}_x [V_{\mathbf{q}}^+ S_{\mathbf{q}}^{(0)} M_{\mathbf{q},\mathbf{b}_x}^{(0)} V_{\mathbf{q}+\mathbf{b}_x} \\ & \quad - V_{\mathbf{q}}^+ S_{\mathbf{q}}^{(0)} V_{\mathbf{q}}] \end{aligned} \quad (49)$$

and

$$\begin{aligned} & \langle u_{\mathbf{q}}^{(W)} | \hat{s}_z \hat{H} | \partial_x u_{\mathbf{q}}^{(W)} \rangle \\ &= \sum_{\mathbf{b}_x} w_{\mathbf{b}_x} \mathbf{b}_x [V_{\mathbf{q}}^+ \langle u_{\mathbf{q}}^{(0)} | \hat{s}_z \hat{H} | u_{\mathbf{q}+\mathbf{b}_x}^{(0)} \rangle V_{\mathbf{q}+\mathbf{b}_x} \\ & \quad - V_{\mathbf{q}}^+ \langle u_{\mathbf{q}}^{(0)} | \hat{s}_z \hat{H} | u_{\mathbf{q}}^{(0)} \rangle V_{\mathbf{q}}] \\ &= \sum_{\mathbf{b}_x} w_{\mathbf{b}_x} \mathbf{b}_x [V_{\mathbf{q}}^+ S_{\mathbf{q}}^{(0)} H_{\mathbf{q}}^{(0)} M_{\mathbf{q},\mathbf{b}_x}^{(0)} V_{\mathbf{q}+\mathbf{b}_x} \\ & \quad - V_{\mathbf{q}}^+ S_{\mathbf{q}}^{(0)} H_{\mathbf{q}}^{(0)} V_{\mathbf{q}}] \end{aligned} \quad (50)$$

The only unknown quantities are $S_{\mathbf{q}}^{(0)} = \langle u_{\mathbf{q}}^{(0)} | \hat{s}_z | u_{\mathbf{q}}^{(0)} \rangle$, $H_{\mathbf{q}}^{(0)} = \langle u_{\mathbf{q}}^{(0)} | \hat{H}_{\mathbf{q}} | u_{\mathbf{q}}^{(0)} \rangle$, $M_{\mathbf{q},\mathbf{b}}^{(0)} = \langle u_{\mathbf{q}}^{(0)} | u_{\mathbf{q}+\mathbf{b}}^{(0)} \rangle$ which are the spin operator matrices, the Hamiltonian matrices and the overlap matrices of the original *ab-initio* wave function, respectively. Note the overlap matrices are available “for free” since they have been computed in the construction process of MLWF. The spin operator matrices and the Hamiltonian matrices are easily computed from *ab-initio* results. The PW2WANNIER90 program, which is the interface between QUANTUM ESPRESSO [23, 24] and WANNIER90 [25], has already calculated these three quantities. Thus by our derivations, no additional quantities are required for computing SHC. For other *ab-initio* software packages, only the Hamiltonian matrix, which is just the eigenvalues, and the spin operator matrices, are the additional quantities that need to be passed to WANNIER90 from *ab-initio* calculation.

At this point, all the needed matrices have been evaluated from the *ab-initio* calculation. In summary, we succeed in computing the four real space matrices $\langle \mathbf{0} | \hat{s}_z | \mathbf{R} \rangle$, $\langle \mathbf{0} | \hat{s}_z (\mathbf{r} - \mathbf{R})_x | \mathbf{R} \rangle$, $\langle \mathbf{0} | \hat{s}_z \hat{H} (\mathbf{r} - \mathbf{R})_x | \mathbf{R} \rangle$ and $\langle \mathbf{0} | \hat{s}_z \hat{H} | \mathbf{R} \rangle$. Then we interpolate these matrices on a dense \mathbf{k} -mesh by the inverse Fourier transform, i.e. the Equ.(35), (36), (37) and (38). Through gauge transformation the $S^{(H)}$, $K^{(H)}$, $L^{(H)}$ are computed. Finally, through Equ.(23) and Equ.(22) the spin current operator matrix is computed. We implemented the computer code for the Kubo formula of SHC on the basis of WANNIER90 package [18, 19, 25].

IV. COMPUTATIONAL DETAILS

To demonstrate the validity of our Wannier interpolation approach, we performed SHC calculations of fcc Pt

and GaAs, which have been investigated by direct evaluation of Kubo formula Equ.(1) based on LMTO method [14, 15]. After that, results of α -Ta and β -Ta are shown.

All the *ab-initio* calculations were performed using QUANTUM ESPRESSO package based on projector-augmented wave (PAW) method and a plane wave basis set [23, 24]. The exchange and correlation terms were described using generalized gradient approximation (GGA) in the scheme of Perdew-Burke-Ernzerhof (PBE) parameterization, as implemented in the PSLIBRARY [26]. Energy convergence criteria of all the calculations were set as 1.0×10^{-8} Ry.

A. dc SHC of fcc Pt

For the *ab-initio* calculations, we used a wave function cutoff of 90 Ry and electron density cutoff of 1080 Ry. In the self-consistent field (scf) calculation, Monkhorst-Pack k-meshes of $6 \times 6 \times 6$ to $14 \times 14 \times 14$ were tested while the non-self-consistent (nscf) k-meshes were kept the same as the scf k-meshes for the construction of MLWF. The fcc unit cell contains one Pt atom and the lattice constant was set as 3.92 Å.

For the construction of MLWF, an inner frozen window of 0.0 eV to 30.0 eV and an outer disentanglement window of 0.0 eV to 60.0 eV were used to extract 18 spinor WFs having the form of *s*, *p* and *d*-like Gaussians [see Fig.1]. The spread of each WF was in the range of 0.7 \AA^2 to 2.3 \AA^2 , and the spreads for both the disentanglement and Wannierization processes were converged under $1 \times 10^{-10} \text{ \AA}^2$.

As can be seen in Fig.1, under the disentanglement frozen window, the *ab-initio* band structure is fully recovered by the MLWFs. Since the Kubo formula Equ.(1) involves unoccupied bands, a large frozen window is needed to ensure those unoccupied bands, which are several eV above the Fermi energy, can be accurately recovered. Thus the distortions of higher energy unoccupied bands have little influence on the calculated SHC.

Comparing with the LMTO results [15], our result of 2280 (\hbar/e)S/cm deviates about 3.6% from that of 2200 (\hbar/e)S/cm. Considering the difference between *ab-initio* methods and softwares, this small deviation is tolerable and confirms that our Wannier interpolation approach is capable of calculating SHC with high accuracy. Varying the position of Fermi level can be viewed as a crude approximation of the doping effect on the SHC. As shown in Fig. 1, the SHC reaches its peak value around the Fermi energy, while drops to -2172 (\hbar/e)S/cm at 4.34 eV below the Fermi energy. The strong resemblance of the Fig.1(b) to the result in Ref. [15] again validates our Wannier interpolation approach.

More insights can be obtained by band projected plot of SHC, as shown in Fig.2. The color in Fig.2(a) is the SHC projected on each band, i.e. the magnitude

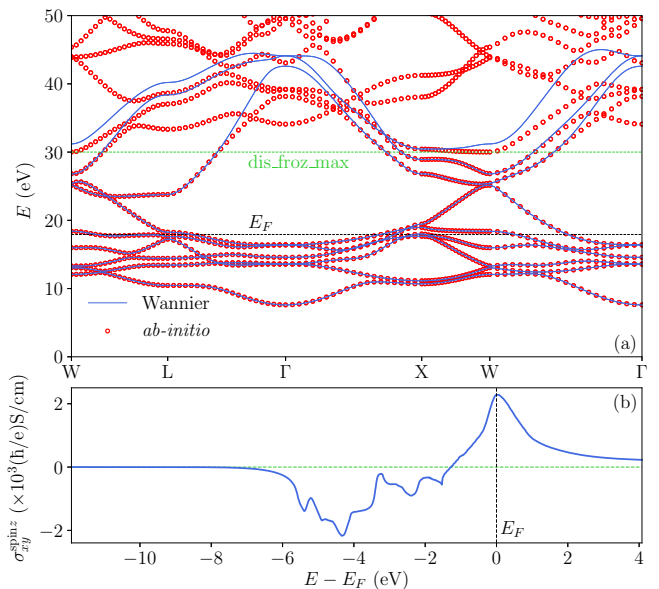


FIG. 1. (a) Comparison of fcc Pt band structure obtained from *ab-initio* calculation (red circles) and the interpolated band structure by MLWFs (blue lines). The black dashed horizontal line corresponds to the Fermi energy, the green dashed horizontal line corresponds to the upper limit of the frozen inner window in the disentanglement process when constructing MLWFs. (b) The SHC variation of fcc Pt with respect to the position of Fermi energy. The black dashed vertical line corresponds to the calculated Fermi energy, at which the SHC reaches 2280 (\hbar/e)S/cm.

of Equ.(3) after taking logarithm,

$$\text{result} = \begin{cases} \text{sgn}(x) \cdot \log_{10} |x|, & |x| > 10, \\ \frac{x}{10}, & |x| \leq 10, \end{cases} \quad (51)$$

where $\text{sgn}(x)$ means taking the sign of x . The SHC is mostly concentrated around *X* point in the BZ. The small spin-orbit splitting induces large SHC variation. The Fig.2(b) is the k-point resolved SHC, i.e. Equ.(4) without \mathbf{k} sum. Spikes near *X* and *L* points contribute to SHC significantly.

A further intuitive analysis can be carried out by plotting k-resolved SHC on a slice of BZ, as shown in Fig. 3. We chose the vector $2\vec{\Gamma L} = (1, 0, 0)$ [in fractional coordinates relative to reciprocal lattice] as the horizontal axis, and the vector $(\frac{\sqrt{2}}{4}, \frac{3\sqrt{2}}{4}, 0)$ as the vertical axis, which lies in the *X*- Γ -*L* plane and is normal to $\vec{\Gamma L}$. The $(\frac{1}{2}, 0, 0)$ point on the horizontal axis is the *L* point, the small red spot around the *L* point is consistent with the band projected result in Fig.2(a). The near-center $(\frac{1}{2}, \frac{1}{2}, 0)$ point corresponds to the *X* point, where rapid variation of SHC occurs.

Since the calculation of SHC always involves k-point mesh on the order of million, special care must be taken to the convergence issues. As shown in the Fig.2 and Fig.3, the rapid variation of SHC usually only occurs at a

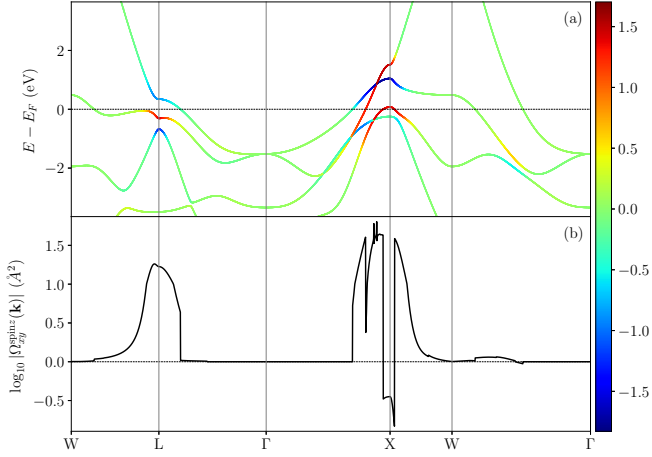


FIG. 2. SHC of fcc Pt along a path in the BZ. The color bar in the panel (a) is the SHC projected on each band after taking logarithm [Equ.(51)], i.e the Equ.(3). The panel (b) is the k -point resolved SHC after taking logarithm [Equ.(51)], i.e. Equ.(4) without \mathbf{k} sum.

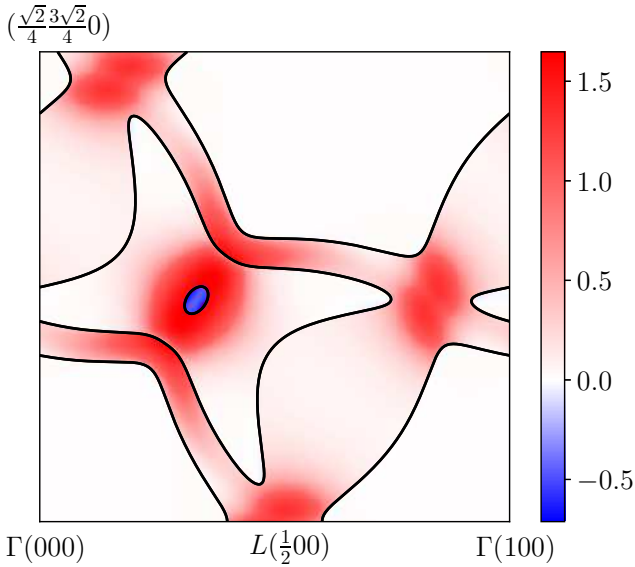


FIG. 3. SHC of fcc Pt in a slice of the BZ. The slice is perpendicular to the reciprocal space c axis. The black lines are the intersection of the slice with the Fermi surface. The horizontal axis is the vector $2\vec{\Gamma L} = (1, 0, 0)$, and the vertical axis is the vector $(\frac{\sqrt{2}}{4}, \frac{3\sqrt{2}}{4}, 0)$, which lies in the $X\text{-}\Gamma\text{-}L$ plane and is normal to $\vec{\Gamma L}$. The $(\frac{1}{2}, 0, 0)$ on the x-axis is the L point and the near-center $(\frac{1}{2}, \frac{1}{2}, 0)$ point [i.e. $(\frac{1}{3}, \frac{\sqrt{2}}{3})$ relative to horizontal and vertical axes] corresponds to the X point. The color represents the logarithm [Equ.(51)] of Equ.(4) without \mathbf{k} sum. The coordinates of the above mentioned vectors are fractional coordinates relative to the reciprocal lattice.

TABLE I. The SHC values and its convergence trend relative to *ab-initio* k-mesh, Wannier interpolation k-mesh, and adaptive refinement k-mesh. All the k-mesh numbers n in each cell of the table should be expanded as $n \times n \times n$. For example the No. 1 corresponds to the calculation performed on $6 \times 6 \times 6$ *ab-initio* k-mesh and $100 \times 100 \times 100$ Wannier interpolation k-mesh without adaptive k-mesh refinement.

No.	ab. k-mesh	Wan. k-mesh	adpt. k-mesh	SHC($(\frac{\hbar}{e})S/cm$)
1	6	100	0	2559.39
2	6	100	2	2281.44
3	6	100	4	2281.44
4	8	40	0	2300.56
5	8	60	0	2270.44
6	8	80	0	2286.38
7	8	100	0	2279.62
8	8	120	0	2282.64
9	8	140	0	2283.84
10	14	200	0	2282.30
11	14	300	0	2281.27

small portion of the full BZ. In such cases, the method of adaptive k-mesh refinement can be very helpful. The convergence of the SHC with respect to the choice of k-mesh is presented in Table I. The value of 2281.27 (\hbar/e)S/cm from the No. 11 calculation is regarded as the fully converged result. Comparing the results No. 1, 2, 3 and 11, we find that the fully converged result can be conveniently obtained by adaptive k-mesh refinement even on a not so dense BZ grid. Comparing the results from No. 4 to 9, it can be concluded that the Wannier interpolation k-mesh is the key parameters for the convergence of SHC. Besides, it is noticeable that the density of the original *ab-initio* k-mesh has little influence on the convergence of SHC. Since in the construction process of MLWF, the *ab-initio* k-mesh is sufficient if well localized real space quantities such as Equ.(42), (43), (44) and (45) are acquired. In fact, the most significant merit of MLWF is that high accuracy interpolated results can be obtained on a relatively coarse *ab-initio* calculation, which eases the computational burden while preserves the accuracy of *ab-initio* calculation. The above mentioned calculation of Pt, which was performed on $8 \times 8 \times 8$ *ab-initio* k-mesh, $100 \times 100 \times 100$ Wannier interpolation k-mesh with $4 \times 4 \times 4$ adaptive refinement k-mesh, spent 492 seconds on 120 CPU cores, which is a bit larger than the total time spent by the scf and nscf calculations for the construction of MLWF.

B. ac SHC of GaAs

We further performed ac SHC calculations of GaAs. In this case, the Monkhorst-Pack k-meshes of $10 \times 10 \times 10$ were used for the scf and nscf calculations. The fcc unit cell contains one Ga atom located at $(0, 0, 0)$ and one As atom located at $(\frac{1}{4}, \frac{1}{4}, \frac{1}{4})$, and the lattice constant was set as 5.654 Å. The *ab-initio* and the Wannier interpolated

band structures are shown in supplemental material [27] Fig. S1. The calculated band gap of 0.40 eV at Γ point is much smaller than the experimental value of 1.52 eV, so we applied a scissors shift of the conduction band so that the experimental band gap can be restored.

For the construction of MLWF, the 10 underlying valence bands are excluded, and 16 WFs are extracted from the 16 bands around the band gap. No disentanglement process is adopted since the 16 bands are isolated. 16 spinor WFs having the form of As located sp^3 -like and Ga located sp^3 -like Gaussians are used [see supplemental material [27] Fig.S1]. The spread of each WF is in the range of 3.6 \AA^2 to 4.7 \AA^2 , and the spread for the Wannierization process was converged under $1 \times 10^{-10} \text{ \AA}^2$. The Wannier interpolated band structure again accurately recovered the *ab-initio* one.

When the frequency ω varies, the denominator in Equ.(1) may approach 0, causing large spikes in the plot. To mitigate this difficulty, two kinds of smearing are adopted, the fixed smearing and adaptive smearing. Follow the method in Ref. [28], the smearing parameter η is set as

$$W_{nm,\mathbf{k}} = a \left| \frac{\partial \mathcal{E}_{n\mathbf{k}}}{\partial \mathbf{k}} - \frac{\partial \mathcal{E}_{m\mathbf{k}}}{\partial \mathbf{k}} \right| \Delta k, \quad (52)$$

which is varied according to the level spacing. The a is the factor of adaptive smearing, and further more the calculated $W_{nm,\mathbf{k}}$ is compared with a fixed value W_{max} to avoid too large smearing parameter. In the calculation of Fig.4, we set $a = 1.414$ and $W_{max} = 1.0 \text{ eV}$, while for fixed smearing we set $W = 0.05 \text{ eV}$. As shown in Fig.4, the adaptive smearing method successfully avoids unphysical reduction of the peaks and kinks, thus the characteristics of Van Hove singularities are well preserved.

Irrespective of the different *ab-initio* method adopted in the calculations, our results of Fig.4 still well match that of Ref. [14], further validating the accuracy of our Wannier interpolation approach.

C. α -Ta and β -Ta

In this section we perform SHC calculations on tantalum. Tantalum has been adopted in many SOT experiments because of its large spin Hall angle (SHA). Two phases of tantalum can exist, i.e. the α -Ta and β -Ta. It is already known that the resistivity of β -Ta, around $200 \mu\Omega\text{cm}$, is approximately 4 times as large as that of α -Ta, which has resistivity around $50 \mu\Omega\text{cm}$ [29, 30]. This partly explains the relatively large SHA of β -Ta, since SHA is proportional to the ratio of SHC $\sigma_{xy}^{\text{spinz}}$ to conductivity σ_{xx} . For a further understanding of Ta SHA, a comparison on SHC of α -Ta and β -Ta is beneficial.

For the *ab-initio* calculations, we used a wave function cutoff of 60 Ry and electron density cutoff of 480 Ry. For the self-consistent field (scf) calculation, Monkhorst-Pack

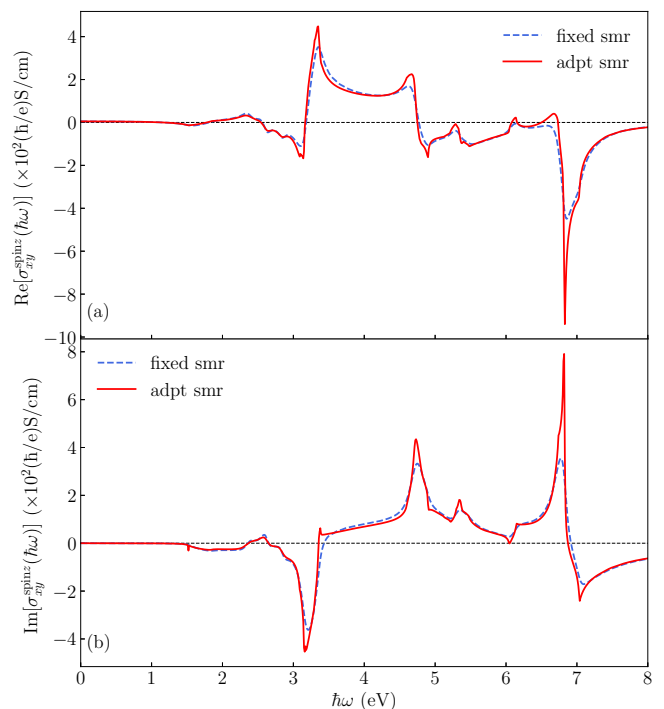


FIG. 4. The (a) real part and (b) imaginary part of GaAs ac SHC. The blue dashed lines correspond to calculation with fixed smearing width of 0.05 eV, while the red solid lines correspond to calculation with adaptive smearing.

k -mesh of $8 \times 8 \times 8$ was used, and the non-self-consistent (nscf) k -mesh was kept the same as the scf k -mesh for the construction of MLWF. The α -Ta has a bcc crystal structure and the lattice constant was set as the relaxed result of 3.322 \AA . For the Wannier interpolation, a k -mesh of $100 \times 100 \times 100$ and an adaptive k -mesh of $10 \times 10 \times 10$ were used. For the calculations of band projected and k -resolved SHC, i.e. Fig.6, 7, S3 and S5 [in supplemental material [27]], a fixed smearing width of 0.05 eV were adopted.

For the construction of MLWF, an inner frozen window of 0.0 eV to 30.0 eV and an outer disentanglement window of 0.0 eV to 50.0 eV were used to extract 18 spinor WFs having the form of d , p and s -like Gaussians [see supplemental material [27] Fig.S2]. The spread of each WF was less than 1.64 \AA^2 , and the spreads for both the disentanglement and Wannierization processes were converged under $1 \times 10^{-10} \text{ \AA}^2$. As can be seen in supplemental material [27] Fig.S2, under the disentanglement frozen window, the *ab-initio* band structure is again fully recovered by the MLWFs.

The variation of SHC with respect to the changes of Fermi energy is shown in Fig. 5(a). The SHC at Fermi energy is $-142 (\hbar/e)\text{S/cm}$, which is an order of magnitude smaller than that of fcc Pt. While at 1 eV above Fermi energy, the SHC reaches its peak value of $-1062 (\hbar/e)\text{S/cm}$. This can be further comprehended by band projected and k -point resolved SHC, as shown

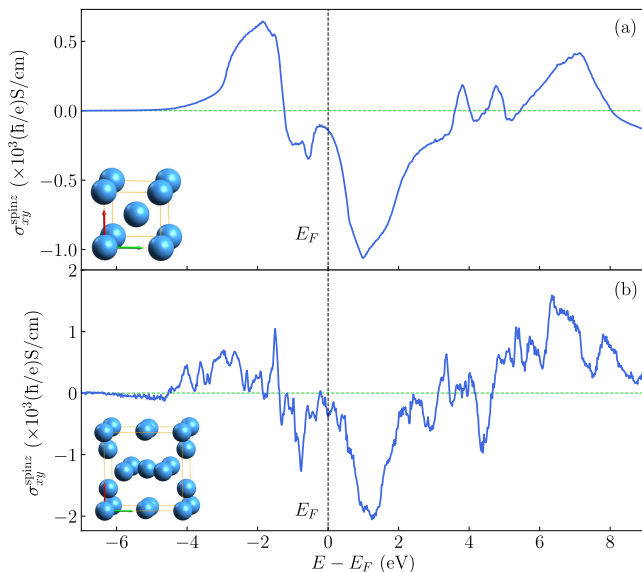


FIG. 5. The variation of SHC with respect to the position of Fermi energy for (a) α -Ta and (b) β -Ta. The black dashed vertical line corresponds to the calculated Fermi energy, at which the SHC reaches -142 (\hbar/e)S/cm for α -Ta and -389 (\hbar/e)S/cm for β -Ta. The inset shows the crystal structures of α -Ta: bcc and β -Ta: tetragonal.

in Fig.6. The contribution to SHC is mostly concentrated around P point and along Γ to H path in the BZ. Band crossings and small spin-orbit-split gaps induce large variations of SHC. When Fermi energy are raised 1 eV higher, the contributions of P point which are located above the Fermi energy, will be included in the sum of Equ.(4). When Fermi energy is raised even higher, contributions with positive sign [red color in Fig.6(a)] will cancel the aforementioned minus sign contributions [blue color in Fig.6(a)]. Thus the peaks appear and then disappear in Fig.5(a). The k -resolved SHC on a slice of BZ, as shown in supplemental material [27] Fig. S3, shows similar characteristics as that of Pt Fig.3. Rapid variations of SHC occurs near Fermi surface, where spin-orbit coupling induces avoided crossings.

We further performed SHC calculation of β -Ta. The case of β -Ta is more complicated than α -Ta. Regarding the crystal structure of β -Ta, models of tetragonal, hexagonal, β -Uranium and etc. have been proposed [31]. Some recent experiments find β -Ta has tetragonal structure [32, 33], thus we adopt tetragonal structure in the SHC calculation of β -Ta, as shown in the inset of Fig.5(b).

The unit cell contains 8 Ta atoms. The lattice constants were set as $a = 5.34$ Å and $c = 4.97$ Å. For the construction of MLWF, an inner frozen window of 0.0 eV to 30.0 eV and an outer disentanglement window of 0.0 eV to 50.0 eV were used to extract 144 spinor WFs having the form of d , p and s -like Gaussians for each Ta atom. A Monkhorst-Pack k -mesh of $4 \times 4 \times 4$ was used in the

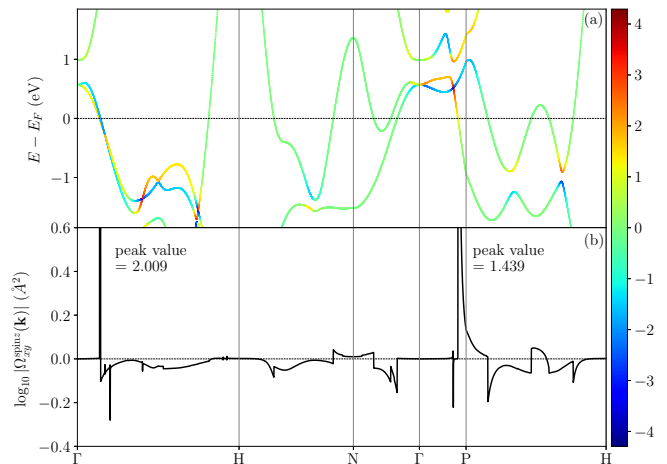


FIG. 6. SHC of α -Ta along a path in the BZ. The color bar in the panel (a) is the SHC projected on each band after taking logarithm [Equ.(51)], i.e the Equ.(3). The panel (b) is the k -point resolved SHC after taking logarithm [Equ.(51)], i.e. Equ.(4) without \mathbf{k} sum.

nsfc calculation and it was found that the spread of each WF was less than 1.86 Å², and the spreads for both the disentanglement and Wannierization processes were converged under 1×10^{-10} Å². For the Wannier interpolation, a k -mesh of $60 \times 60 \times 60$ and an adaptive k -mesh of $6 \times 6 \times 6$ were used. The Wannier interpolated band structure again accurately recovered the *ab-initio* one, shown in supplemental material Fig.S4.

Unlike the case of α -Ta, the variation of SHC relative to the position of Fermi energy shows more complex behavior. The SHC at Fermi energy is -389 (\hbar/e)S/cm, still an order of magnitude smaller than that of fcc Pt, but 2.7 times of α -Ta. While at 1.238 eV above Fermi energy, the SHC reaches its peak value of -2055 (\hbar/e)S/cm. The bands around Fermi energy are mainly composed of d states, where considerable numbers of band crossings and spin-orbit-split gaps induce large changes of SHC, consistent with the band projected SHC as shown in Fig.7(a). k -resolved SHC on a slice of BZ is shown in supplemental material [27] Fig. S5. Same as before, rapid variations of SHC happen again in the vicinity of Fermi surface.

In summary, SHC of β -Ta is -389 (\hbar/e)S/cm, while that of α -Ta is -142 (\hbar/e)S/cm. The SHC of β -Ta is 2.7 times of α -Ta, combined with the larger resistivity of β -Ta, resulting in the larger SHA. Based on experimental results of resistivity $\rho_{xx}^{\alpha\text{-Ta}} \simeq 50$ $\mu\Omega\text{cm}$ and $\rho_{xx}^{\beta\text{-Ta}} \simeq 200$ $\mu\Omega\text{cm}$, we can evaluate the SHA according to

$$\theta_{SH} = \frac{2e}{\hbar} \frac{\sigma_{xy}}{\sigma_{xx}}. \quad (53)$$

The results are $\theta_{SH}^{\alpha\text{-Ta}} \simeq -0.0142$ and $\theta_{SH}^{\beta\text{-Ta}} \simeq -0.156$. The magnitude of $\theta_{SH}^{\beta\text{-Ta}}$ is quite consistent with the experimental value of 0.12 to 0.15 [2]. Considering the

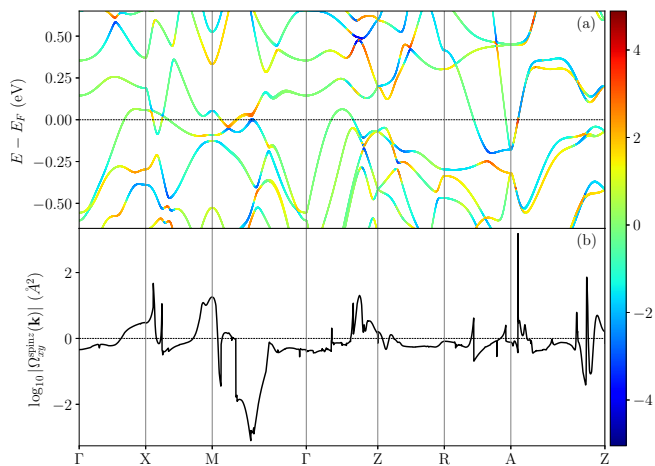


FIG. 7. SHC of β -Ta along a path in the BZ. The color bar in the panel (a) is the SHC projected on each band after taking logarithm [Equ.(51)], i.e the Equ.(3). The panel (b) is the k-point resolved SHC after taking logarithm [Equ.(51)], i.e. Equ.(4) without \mathbf{k} sum.

resistivity of Ta is located near the good metal regime of $\sigma_{xx} \simeq 10^4$ - 10^6 S/cm [1, 34], the intrinsic contribution should dominate so the experimental result can be readily reproduced by our calculation. Moreover, the signs of SHC for both α -Ta and β -Ta are opposite to that of fcc Pt, and this sign difference has been verified by experiment [2, 33]. In addition, it is worth mentioning that the SHC of both α -Ta and β -Ta reach its peak at around 1 eV above their respective Fermi energy, doping or alloying with other materials may shift the Fermi energy to reach the maximum SHC.

V. SUMMARY

The Wannier interpolation approach for the Kubo formula of intrinsic SHC is developed to achieve high accuracy and efficiency. The results of Pt dc SHC and GaAs ac SHC are validated against previous works by direct evaluating Kubo formula, and SHC of α -Ta and β -Ta are calculated based on the Wannier interpolation approach. It is found that SHC of β -Ta is 2.7 times of α -Ta, while both have the opposite sign relative to fcc Pt and are an order of magnitude smaller than Pt. Moreover, based on experimental data of resistivity, our calculated spin Hall

angle of β -Ta is -0.156, quite consistent with spin Hall angle measured in experiment. This further implies that intrinsic contribution dominates in the spin Hall effect of β -Ta.

The calculations are performed in four consecutive steps. First, a self-consistent calculation produces the converged charge densities. Second, a non-self-consistent calculation is performed on a regular k-mesh and three matrices are computed, which are the spin operator matrix, the overlap matrix and the Hamiltonian matrix. Third, the maximally localized Wannier functions are constructed. Finally, the Kubo formula is interpolated on a dense k-mesh by MLWF to obtain converged results. Due to the merit of real space localization, the fourth interpolation step is very efficient compared with “brute-force” *ab-initio* calculation on the dense k-mesh.

To facilitate the convergence of SHC, adaptive refinement of k-mesh is implemented. The rapid variations of SHC, which are usually located in small portion of the full Brillouin zone, can be captured by the adaptive k-mesh refinement effectively. Since calculations based on LDA/GGA exchange correlation potentials often predict smaller band gaps than experiments, we implement scissors shift in the calculation of SHC to rectify this deviation. To improve convergence in ac SHC calculations, adaptive smearing is implemented and the GaAs calculation shows desirable results.

This Wannier interpolation approach serves as a post-processing step to economically calculate SHC. The ultimate accuracy of the calculated SHC is determined by the underlying *ab-initio* code, since the MLWFs are constructed to provide lossless interpolation of physical quantities in the energy range of interest. The construction of MLWF is independent from the choice of the underlying code, thus our derivation and implementation of Wannier interpolation for SHC are able to co-operate seamlessly with different *ab-initio* algorithms and implementations.

ACKNOWLEDGMENTS

The authors gratefully acknowledge the National Natural Science Foundation of China (Grant No. 61627813, 61571023), the International Collaboration Project B16001, and the National Key Technology Program of China 2017ZX01032101 for their financial support of this work.

-
- [1] J. Sinova, S. O. Valenzuela, J. Wunderlich, C. Back, and T. Jungwirth, *Rev. Mod. Phys.* **87**, 1213 (2015).
 [2] L. Liu, O. J. Lee, T. J. Gudmundsen, D. C. Ralph, and R. A. Buhrman, *Phys. Rev. Lett.* **109**, 096602 (2012).
 [3] L. Liu, C.-F. Pai, Y. Li, H. W. Tseng, D. C. Ralph, and R. A. Buhrman, *Science* **336**, 555 (2012).
 [4] K. Garello, I. M. Miron, C. O. Avci, F. Freimuth,

- Y. Mokrousov, S. Blügel, S. Auffret, O. Boulle, G. Gaudin, and P. Gambardella, *Nat. Nanotechnol.* **8**, 587 (2013).
 [5] A. Manchon and S. Zhang, *Phys. Rev. B* **79**, 094422 (2009).
 [6] N. Sato, F. Xue, R. M. White, C. Bi, and S. X. Wang, *Nat. Electron.* **1**, 508 (2018).

- [7] S. Murakami, N. Nagaosa, and S.-C. Zhang, *Science* **301**, 1348 (2003).
- [8] J. Sinova, D. Culcer, Q. Niu, N. A. Sinitsyn, T. Jungwirth, and A. H. MacDonald, *Phys. Rev. Lett.* **92**, 126603 (2004).
- [9] L. Wang, R. J. H. Wesselink, Y. Liu, Z. Yuan, K. Xia, and P. J. Kelly, *Phys. Rev. Lett.* **116**, 196602 (2016).
- [10] Y. Yao and Z. Fang, *Phys. Rev. Lett.* **95**, 156601 (2005).
- [11] M. Gradhand, D. V. Fedorov, F. Pientka, P. Zahn, I. Mertig, and B. L. Györfy, *J. Phys.: Condens. Matter* **24**, 213202 (2012).
- [12] L. Matthes, S. Kűfner, J. Furthműller, and F. Bechstedt, *Phys. Rev. B* **94**, 085410 (2016).
- [13] Y. Yao, L. Kleinman, A. H. MacDonald, J. Sinova, T. Jungwirth, D.-s. Wang, E. Wang, and Q. Niu, *Phys. Rev. Lett.* **92**, 037204 (2004).
- [14] G. Y. Guo, Y. Yao, and Q. Niu, *Phys. Rev. Lett.* **94**, 226601 (2005).
- [15] G. Y. Guo, S. Murakami, T. W. Chen, and N. Nagaosa, *Phys. Rev. Lett.* **100**, 096401 (2008).
- [16] Y. Sun, Y. Zhang, C. Felser, and B. Yan, *Phys. Rev. Lett.* **117**, 146403 (2016).
- [17] X. Wang, J. R. Yates, I. Souza, and D. Vanderbilt, *Phys. Rev. B* **74**, 195118 (2006).
- [18] N. Marzari and D. Vanderbilt, *Phys. Rev. B* **56**, 12847 (1997).
- [19] I. Souza, N. Marzari, and D. Vanderbilt, *Phys. Rev. B* **65**, 035109 (2001).
- [20] N. Marzari, A. A. Mostofi, J. R. Yates, I. Souza, and D. Vanderbilt, *Rev. Mod. Phys.* **84**, 1419 (2012).
- [21] M. G. Lopez, D. Vanderbilt, T. Thonhauser, and I. Souza, *Phys. Rev. B* **85**, 014435 (2012).
- [22] X. Wang, D. Vanderbilt, J. R. Yates, and I. Souza, *Phys. Rev. B* **76**, 195109 (2007).
- [23] P. Giannozzi, S. Baroni, N. Bonini, M. Calandra, R. Car, C. Cavazzoni, D. Ceresoli, G. L. Chiarotti, M. Cococcioni, I. Dabo, and *et al.*, *J. Phys.: Condens. Matter* **21**, 395502 (2009).
- [24] P. Giannozzi, O. Andreussi, T. Brumme, O. Bunau, M. B. Nardelli, M. Calandra, R. Car, C. Cavazzoni, D. Ceresoli, M. Cococcioni, and *et al.*, *J. Phys.: Condens. Matter* **29**, 465901 (2017).
- [25] A. A. Mostofi, J. R. Yates, G. Pizzi, Y. S. Lee, I. Souza, D. Vanderbilt, and N. Marzari, *Comput. Phys. Commun.* **185**, 2309 (2014).
- [26] A. D. Corso, *Comput. Mater. Sci.* **95**, 337 (2014).
- [27] See Supplemental Material at [URL will be inserted by publisher].
- [28] J. R. Yates, X. Wang, D. Vanderbilt, and I. Souza, *Phys. Rev. B* **75**, 195121 (2007).
- [29] M. H. Read and C. Altman, *Appl. Phys. Lett.* **7**, 51 (1965).
- [30] L. A. Clevenger, A. Mutscheller, J. M. E. Harper, C. Cabral, and K. Barmak, *J. Appl. Phys.* **72**, 4918 (1992).
- [31] A. Jiang, A. Yohannan, N. O. Nnolim, T. A. Tyson, L. Axe, S. L. Lee, and P. Cote, *Thin Solid Films* **437**, 116 (2003).
- [32] C. Hahn, G. de Loubens, O. Klein, M. Viret, V. V. Naleto, and J. Ben Youssef, *Phys. Rev. B* **87**, 174417 (2013).
- [33] R. Yu, B. F. Miao, L. Sun, Q. Liu, J. Du, P. Omelchenko, B. Heinrich, M. Wu, and H. F. Ding, *Phys. Rev. Mater.* **2**, 074406 (2018).
- [34] N. Nagaosa, J. Sinova, S. Onoda, A. H. MacDonald, and N. P. Ong, *Rev. Mod. Phys.* **82**, 1539 (2010).